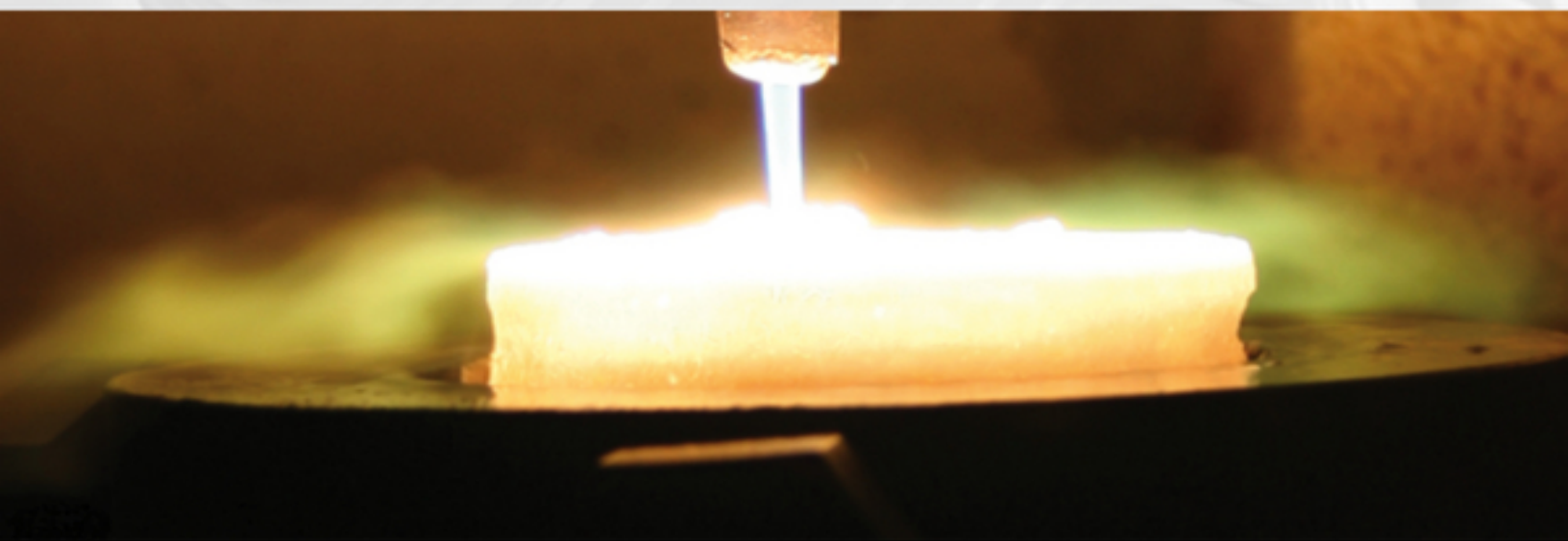


# ULTRA-HIGH TEMPERATURE CERAMICS

**MATERIALS FOR EXTREME  
ENVIRONMENT APPLICATIONS**



EDITED BY

WILLIAM G. FAHRENHOLTZ  
ERIC J. WUCHINA  
WILLIAM E. LEE  
YANCHUN ZHOU

# CONTENTS

[Cover](#)

[Title page](#)

[Copyright page](#)

[Dedication page](#)

[Acknowledgments](#)

[Contributors List](#)

[1 Introduction](#)

[1.1 Background](#)

[1.2 Ultra-High Temperature Ceramics](#)

[1.3 Description of Contents](#)

[References](#)

[2 A Historical Perspective on Research Related to Ultra-High Temperature Ceramics](#)

[2.1 Ultra-High Temperature Ceramics](#)

[2.2 Historic Research](#)

[2.3 Initial NASA Studies](#)

[2.4 Research Funded by the Air Force Materials Laboratory](#)

[2.5 Summary](#)

[Acknowledgments](#)

[References](#)

[3 Reactive Processes for Diboride-Based Ultra-High Temperature Ceramics](#)

[3.1 Introduction](#)

[3.2 Reactive Processes for the Synthesis of Diboride Powders](#)

[3.3 Reactive Processes for Oxygen Removing during Sintering](#)

[3.4 Reactive Sintering Processes](#)

[3.5 Summary](#)

[References](#)

[4 First-Principles Investigation on the Chemical Bonding and Intrinsic Elastic Properties of Transition Metal Diborides  \$TMB\_2\$  \(TM=Zr, Hf, Nb, Ta, and Y\)](#)

[4.1 Introduction](#)

[4.2 Calculation Methods](#)

[4.3 Results and Discussion](#)

[4.4 Conclusion Remarks](#)

[Acknowledgment](#)

[References](#)

[5 Near-Net-Shaping of Ultra-High Temperature Ceramics](#)

[5.1 Introduction](#)

[5.2 Understanding Colloidal Systems: Interparticle Forces](#)

[5.3 Near-Net-Shape Colloidal Processing Techniques](#)

[5.4 Summary, Recommendations, and Path Forward](#)

[Acknowledgments](#)

[References](#)

[6 Sintering and Densification Mechanisms of Ultra-High Temperature Ceramics](#)

[6.1 Introduction](#)

[6.2  \$MB\_2\$  with Metals](#)

[6.3  \$MB\_2\$  with Nitrides](#)

[6.4  \$MB\_2\$  with Metal Disilicides](#)

[6.5 MB<sub>2</sub> with Carbon or Carbides](#)

[6.6 MB<sub>2</sub> with SiC](#)

[6.7 MB<sub>2</sub>-SiC Composites with Third Phases](#)

[6.8 Effects of Sintering Aids on High-Temperature Stability](#)

[6.9 Transition Metal Carbides](#)

[6.10 Conclusions](#)

[Acknowledgments](#)

[References](#)

[7 UHTC Composites for Hypersonic Applications](#)

[7.1 Introduction](#)

[7.2 Preparation of Continuous-Fiber-Reinforced UHTC Composites](#)

[7.3 UHTC Coatings](#)

[7.4 Short-Fiber-Reinforced UHTC Composites](#)

[7.5 Hybrid UHTC Composites](#)

[7.6 Summary and Future Prospects](#)

[References](#)

[8 Mechanical Properties of Zirconium-Diboride Based UHTCs](#)

[8.1 Introduction](#)

[8.2 Room Temperature Mechanical Properties](#)

[8.3 Elevated-Temperature Mechanical Properties](#)

[8.4 Concluding Remarks](#)

[References](#)

[9 Thermal Conductivity of ZrB<sub>2</sub> and HfB<sub>2</sub>](#)

[9.1 Introduction](#)

[9.2 Conductivity of ZrB<sub>2</sub> and HfB<sub>2</sub>](#)

[9.3 ZrB<sub>2</sub> and HfB<sub>2</sub> Composites](#)

[9.4 Electron and Phonon Contributions to Thermal Conductivity](#)

[9.5 Concluding Remarks](#)

[References](#)

[10 Deformation and Hardness of UHTCs as a Function of Temperature](#)

[10.1 Introduction](#)

[10.2 Elastic Properties](#)

[10.3 Hardness](#)

[10.4 Hardness and Yield Strength](#)

[10.5 Deformation Mechanism Maps](#)

[10.6 Lattice Resistance to Dislocation Glide](#)

[10.7 Dislocation Glide Controlled by Other Obstacles](#)

[10.8 Deformation by Creep](#)

[10.9 Deformation of Carbides versus Borides](#)

[10.10 Conclusions](#)

[References](#)

[11 Modeling and Evaluating the Environmental Degradation of UHTCs under Hypersonic Flow](#)

[11.1 Introduction](#)

[11.2 Oxidation Modeling](#)

[11.3 UHTC Behavior under Simulated Hypersonic Conditions](#)

[11.4 Comparing Model Predictions to Leading-Edge Behavior](#)

[11.5 Behavior of UHTCs under Other Test Methods](#)

[11.6 Summary](#)

[References](#)

## 12 Tantalum Carbides: Their Microstructures and Deformation Behavior

12.1 Crystallography of Tantalum Carbides

12.2 Microstructures of Tantalum Carbides

12.3 Mechanical Properties of Tantalum Carbides

12.4 Summary

Acknowledgments

References

## 13 Titanium Diboride

13.1 Introduction

13.2 Phase Diagram, Crystal Structure, and Bonding

13.3 Synthesis of Titanium Diboride Powders

13.4 Densification of Transition Metal Borides

13.5 Mechanical Properties at Ambient and Elevated Temperatures

13.6 Physical Properties and Oxidation Resistance

13.7 Oxidation Resistance

13.8 Tribological Properties

13.9 Applications of TiB<sub>2</sub>

13.10 Conclusions

References

## 14 The Group IV Carbides and Nitrides

14.1 Background

14.2 Group IV Carbides

14.3 Preparation and Processing

14.4 Mechanical and Physical Properties

14.5 Oxidation of the UHTC Carbides and Nitrides

14.6 Oxidation of the UHTC Carbides

14.7 UHTC Nitrides

[14.8 Preparation, Diffusion, and Phase Formation](#)

[14.9 Mechanical and Physical Properties](#)

[14.10 Oxidation of Nitrides](#)

[14.11 Conclusions and Future Research](#)

[Acknowledgments](#)

[References](#)

[15 Nuclear Applications for Ultra-High Temperature Ceramics and MAX Phases](#)

[15.1 Future Nuclear Reactors](#)

[15.2 Current Nuclear Ceramics](#)

[15.3 Future Nuclear Ceramics](#)

[15.4 Non-Oxide Nuclear Fuels](#)

[15.5 Other Possible Future Fission and Fusion Applications](#)

[15.6 Thermodynamics of Nuclear Systems](#)

[15.7 Conclusions](#)

[References](#)

[16 UHTC-Based Hot Structures](#)

[16.1 Introduction](#)

[16.2 TPS: Test Articles and Prototypes](#)

[16.3 Plasma Tests of Nose Test Articles](#)

[16.4 Expert Project: Computational Fluid Dynamics Computations and Plasma Tests](#)

[16.5 In-Fling Testing of the Capsule "SHARK"](#)

[16.6 Future Work](#)

[References](#)

[Index](#)

[End User License Agreement](#)

# List of Tables

## Chapter 02

[Table 2.1. Selected recommendations for future research and development activities related to UHTCs from Reference \[10\]](#)

[Table 2.2. Compositions examined in the second series of studies by ManLabs \[54\]](#)

[Table 2.3. Summary of compositions studied for the third series of ManLabs projects](#)

## Chapter 03

[Table 3.1. Thermodynamics of the main reactions including the temperatures at which the reactions become favorable at standard state and under mild vacuum](#)

## Chapter 04

[Table 4.1. Lattice constants and bond lengths of  \$TMB\_2\$](#)

[Table 4.2. Second-order elastic constants \( \$c\_{ij}\$ \) and bulk modulus B, Young's modulus E, shear modulus G of  \$TMB\_2\$  \(TM = Y, Zr, Hf, Nb, and Ta\).](#)

## Chapter 05

[Table 5.1 Influence of surface forces on suspension behavior](#)

[Table 5.2 Isoelectric point \(IEP\) of most commonly used UHTCs and other relevant powders](#)

## Chapter 06

[Table 6.1. Sintering agents and corresponding hot pressing temperature ranges \( \$T\_{MAX}\$ \) for  \$ZrB\_2\$  and](#)

## HfB<sub>2</sub>

Table 6.2. MB<sub>2</sub>-MeSi<sub>2</sub> composites reached specific final relative density (rd) using different amounts of MeSi<sub>2</sub>, sintering techniques (Tech), and peak temperatures (T<sub>MAX</sub>).

Table 6.3. ZrB<sub>2</sub>-SiC<sub>W</sub> and ZrB<sub>2</sub>-SiC<sub>F</sub> composites (W: whisker, F: fiber) sintered by hot pressing (HP) using different sintering aids (s.a): peak temperature (T<sub>MAX</sub>), and final relative density (rd).

Table 6.4. ZrB<sub>2</sub>-xSiC<sub>P</sub> composites (P: particulates) densified by HP, SPS, or PS using different sintering aids (s.a): peak temperature (T<sub>MAX</sub>), and final relative density (rd).

Table 6.5. Literature overview of sintering techniques (Tech), parameters, and additives adopted for sintering of MC-composites

## Chapter 08

Table 8.1. Elastic modulus, Vickers hardness, fracture toughness by direct crack method, and four-point flexure strength of ZrB<sub>2</sub> ceramics with and without sintering additives

Table 8.2. Summary of various fitted models of elastic modulus as a function of porosity for ZrB<sub>2</sub>

Table 8.3. Elastic modulus, Vickers hardness, fracture toughness by direct crack method, and four-point flexure strength of ZrB<sub>2</sub>-SiC ceramics

Table 8.4. Elastic modulus, Vickers hardness, fracture toughness by direct crack method, and four-point flexure strength of ZrB<sub>2</sub>-SiC ceramics with various additives

[Table 8.5. Elastic modulus, Vickers hardness, fracture toughness by direct crack method, and four-point flexure strength of  \$ZrB\_2-\(Zr, Mo, Ta\)Si\_2\$  ceramics](#)

## Chapter 09

[Table 9.1. Thermal conductivity of pure  \$ZrB\_2\$  with information on starting/final materials, processing, and density.](#)

[Table 9.2. Summary of solid solution effects on thermal conductivity of  \$ZrB\_2\$](#)

[Table 9.3. Thermal conductivity of pure  \$HfB\_2\$  with information on starting/final materials, processing, and density.](#)

[Table 9.4. Thermal conductivity of  \$ZrB\_2\$ -SiC with information on starting/final materials, processing, and density.](#)

[Table 9.5. Thermal conductivity of two-phase  \$ZrB\_2\$ -based composites with information on starting/final materials, processing, and density.](#)

[Table 9.6. Thermal conductivity of three- and 4-phase  \$ZrB\_2\$ -based composites with information on starting/final materials, processing, and density.](#)

[Table 9.7. Thermal conductivity of  \$HfB\_2\$ -SiC with information on starting/final materials, processing, and density.](#)

[Table 9.8. Thermal conductivity of  \$HfB\_2\$ -based composites with information on starting/final materials, processing, and density.](#)

## Chapter 10

Table 10.1. Elastic constants ( $C_{11}$ ,  $C_{12}$ , and  $C_{44}$ ) and elastic properties of UHTC carbides with the cubic rock salt structure (NaCl, Fm-3 m), with  $K$  as the bulk modulus and  $E_{\text{avg}}$  the average Young's modulus over all orientations

Table 10.2. Elastic constants ( $C_{11}$ ,  $C_{12}$ , and  $C_{44}$ ) and elastic properties of UHTC nitrides with the cubic rock salt structure (NaCl, Fm-3 m), with  $K$  as the bulk modulus and  $E_{\text{avg}}$  the average Young's modulus over all orientations

Table 10.3. Elastic constants and elastic properties of UHTC borides with the hexagonal structure (P6/mmm), with  $K$  as the bulk modulus and  $E_{\text{avg}}$  the average Young's modulus over all orientations

Table 10.4. Rate of decay of the elastic modulus with temperature

Table 10.5. Average shear modulus ( $G$ ), Peierls stress ( $\tau_p$ ), activation energy ( $Q$ ), slip planes, and Burgers vector ( $\mathbf{b}$ ) for UHTCs

Table 10.6. Parameters used to construct the deformation mechanism maps. Parameters for  $\text{ZrB}_2$  from Ref. [63] and for  $\text{ZrC}$  from Ref. [62]. Where the treatment deviates from Ashby and Frost, parameters were adapted to get coincidence of the maps.

## Chapter 12

Table 12.1. Experimentally determined elastic constants of polycrystalline TaC

Table 12.2. Cubic elastic constants and lattice constants of TaC single crystals obtained from experiments and simulation

## Chapter 13

[Table 13.1. Basic physical, mechanical, and oxidation properties of TiB<sub>2</sub>, as well as the other popular Ultra-High-temperature transition metal borides \[1-4\]](#)

[Table 13.2. Summary of densification, microstructure, and mechanical properties of TiB<sub>2</sub> and other transition metal borides](#)

[Table 13.3. Summary of variation of hardness with respect to temperature for TiB<sub>2</sub>-based ceramics with different compositions and processing conditions](#)

[Table 13.4. The effects of temperature on strength of TiB<sub>2</sub> and other transition metal diborides \[4-point \(4-P\) and 3-point \(3-P\) flexural strength\]](#)

[Table 13.5. Summary of thermal conductivity as a function of temperature for TiB<sub>2</sub> ceramics](#)

## Chapter 14

[Table 14.1. Materials with melting temperatures above 3000°C](#)

[Table 14.2. Selected eutectic temperatures \(°C\)](#)

## Chapter 15

[Table 15.1. The GIF reactor designs](#)

[Table 15.2. Typical properties of some current nuclear ceramics](#)

[Table 15.3. Typical properties of UHTCs](#)

[Table 15.4. Typical properties of MAX phases](#)

[Table 15.5. Properties of carbide and nitride fuels](#)

## Chapter 16

[Table 16.1. Thermomechanical and physical properties of ZrB<sub>2</sub> + 15 vol% SiC + 2 vol% MoSi<sub>2</sub>](#)

[\(ZS\) and  \$ZrB\_2 + 10 \text{ vol\% HfB}\_2 + 15 \text{ vol\% SiC} + 2 \text{ vol\% MoSi}\_2\$  \(ZHS\) formulations \[45\]](#)

[Table 16.2. Ceramic formulations and related densification processes: hot-pressing \(HP\) and pressureless sintering \(PLS\).](#)

[Table 16.3. Thermomechanical properties of massive  \$Si\_3N\_4 + 35 \text{ vol\% MoSi}\_2 + 2.5 Y\_2O\_3 + 1 Al\_2O\_3\$  \(RAY2535\).](#)

[Table 16.4. Thermomechanical properties of massive  \$ZrB\_2 + 15 \text{ vol\% SiC} + 10 \text{ vol\% LaB}\_6\$  \[59\]](#)

[Table 16.5. Experimental flow conditions during plasma test on the qualification model EXPERT PL15](#)

## List of Illustrations

### Chapter 01

[Figure 1.1. Materials with the highest reported melting temperature grouped by material family.](#)

### Chapter 02

[Figure 2.1. Summary of types of thermal protection systems as a function of heat flux and exposure time from Reference \[10\].](#)

[Figure 2.2. Strength as a function of temperature for several engineering materials along with a clearly defined Ultra-High temperature regime from Reference \[20\].](#)

[Figure 2.3. Notional temperature requirements for orbital reentry vehicles based on projected wing loading and hypersonic lift-to-drag \(L/D\) ratio from Reference \[41\].](#)

Figure 2.4. Trajectories and methods for dealing with heat loads from Reference [41].

Figure 2.5. Comparison of kinetic rate constants for the oxidation of  $ZrB_2$  and  $HfB_2$  as a function of temperature [45].

Figure 2.6. Relative density as a function of sintering time for  $ZrB_2$  with different B/Me ratios [53].

Figure 2.7. Analysis of densification behavior of  $ZrB_2$  (B/Me ratio = 1.89) as a function of densification temperature where t is sintering time and GS is grain size [53].

Figure 2.8. Oxide-scale thickness as a function of oxidation temperature for  $HfB_2$ , SiC, and  $HfB_2$  containing 20 vol% SiC based on data from Reference [55].

Figure 2.9. Strength as a function of temperature for nominally pure  $ZrB_2$  (Material I) [56].

Figure 2.10. Strength as a function of SiC content in composition IV ( $HfB_2$ -SiC) [56].

Figure 2.11. Thermal conductivity of composition I (nominally pure  $ZrB_2$ ) as a function of temperature using two methods, cut bar for temperatures below 1000°C and thermal flash for temperature above 1000°C. The materials were nominally fully dense with a grain size of  $\sim 20 \mu m$  [57].

Figure 2.12. Schematic of the system built for cold gas/hot wall testing at high gas velocities. The system consisted of an induction heater and high-velocity gas-handling unit [58].

Figure 2.13. Schematic of the 10 MW Arc Splash Facility at AVCO [59].

Figure 2.14. Summary of the results of furnace kinetic studies based on the recession of the parent material after 2 h. HfB<sub>2</sub> is always marginally better than the corresponding ZrB<sub>2</sub> composition. Carbides are not good at “moderate temperature, but extend temperature to higher values. JTA = graphite grade with ZrB<sub>2</sub> and Si additions. KT-SiC = Si-rich SiC (9 vol% free Si). SiO<sub>2</sub> + W = SiO<sub>2</sub> + 60 wt% W. JTO992 is C-HfC-SiC and JTO981 is C-ZrC-SiC [60].

Figure 2.15. Schematic description of the temperature gradients observed across the oxide scales for specimens tested in (left) an arc plasma facility that uses hot gas, cold wall, and high velocity; (center) conventional tube furnace with low velocity flow; and (right) inductively heated specimen in cold gas/hot wall/high velocity [61].

Figure 2.16. Schematic with information about a model trajectory for a lifting body reentry vehicle showing stagnation pressure and enthalpy along with other information for a vehicle with a 3-in. leading-edge radius [61].

Figure 2.17. Comparison of measured recession rates (points) as a function of heat flux and total enthalpy. Lines are shown for a calculated surface temperature of 6100°F (3300°C) under two different conditions. The plot also includes a line (- - -) showing the speed and altitude of a potential reentry trajectory [62].

Figure 2.18. Schematic of the Pirani furnace used for melting point determinations [64].

Figure 2.19. Comparison of melting temperature as a function of composition in the HfC-TaC system for data from Rudy [64] and Agte [65].

[Figure 2.20. Lattice parameter as a function of Ta to Ti ratio and carbon content for the TiC-TaC system \[66\].](#)

[Figure 2.21. Liquidus project for the Zr-B-C ternary phase diagram \[66\].](#)

## Chapter 03

[Figure 3.1. The life cycle of diboride-based ceramics.](#)

[Figure 3.2. Roadmap of the fabrication process of MeB<sub>2</sub> discussed in this chapter.](#)

[Figure 3.3. Standard free energy of reactions as a function of temperature \[4\].](#)

[Figure 3.4. TEM image of the submicrometer ZrB<sub>2</sub> powder by RWR \[10\].](#)

[Figure 3.5. Calculated vapor pressure of B<sub>2</sub>O<sub>3</sub> as a function of temperature in the pressure range maintained in the sintering furnace \[15\].](#)

[Figure 3.6. Molar content of the products calculated by reactions between 3 mole MeC and 1 mole ZrO<sub>2</sub> as a function of the temperature at a vacuum level of 5 Pa: \(a\) WC, \(b\) VC, \(c\) NbC, \(d\) TiC, \(e\) TaC, and \(f\) HfC \[28\].](#)

[Figure 3.7. SEM images of indentation crack propagation in ZrB<sub>2</sub>-SiC-WC ceramics by Zou et al. \[29\]](#)

[Figure 3.8. \(a\) The flexural strength of ZrB<sub>2</sub>-SiC \(ZS\), ZrB<sub>2</sub>-SiC-WC \(ZSW\), and ZrB<sub>2</sub>-SiC-ZrC \(ZSZ\) as a function of testing temperature, \(b\) the load-displacement curves for ZS, ZSW, and ZSZ at 1600°C \[35\].](#)

Figure 3.9. Microstructure formation mechanism of the  $ZrB_2$ -SiC composite in the reaction-synthesis process, depicting the transformation from (a) the powder compact to (b) the final microstructure of the composite [36].

Figure 3.10. Microstructure formation mechanism of  $ZrB_2$ -ZrC-SiC composites in the reaction-synthesis process, depicting conversion from (a) the powder compact to (b) the intermediate state, and (c) the final microstructure [37].

Figure 3.11. Backscattered electron images of the cross section of a typical  $ZrB_2$ -platelet-reinforced ZrC product taken approximately 2 mm from the top (a) and bottom (b) of a 12.7-mm-thick part. The darkest phase is  $ZrB_2$ , the gray phase is ZrC, and the lightest phase is zirconium metal [54].

Figure 3.12.  $ZrB_2$  JCPDS 35-0741 reference (a) and XRD patterns of cross section (b) and sintered surface (c) surface of the PECS samples [43].

Figure 3.13. (a and b) TEM image of  $ZrB_2$  platelet grains at different magnifications; (c) selected-area electron diffraction pattern of platelet grains of (b); (d and e) SEM images of polished surfaces before and after hot forging; (f and g) SEM images of fractured surface before and after hot forging [62].

## Chapter 04

Figure 4.1. Crystal structure of  $TMB_2$ .

Figure 4.2. Pressure dependence of lattice constants  $a$  and  $c$  of  $TMB_2$ .

Figure 4.3. Pressure dependence of TM-B and B-B bond lengths.

Figure 4.4. Electron density difference maps on planes parallel to (0001) that are across Zr (a) and B (b) atoms, and on (11 $\bar{2}$ 0) that is across both Zr and B atoms (c).

Figure 4.5. Band structure of TMB<sub>2</sub>: (a) YB<sub>2</sub>, (b) ZrB<sub>2</sub>, (c) HfB<sub>2</sub>, (d) NbB<sub>2</sub>, and (e) TaB<sub>2</sub>.

Figure 4.6. (a) Total and projected electronic density of states of YB<sub>2</sub>, and decomposed charge density on (11 $\bar{2}$ 0) plane in the energy range from -10.6 to -7.1 eV (b), from -6.6 to -2.0 eV (c), from -4.3 to 0.45 eV (d), from -2.3 to 0.45 eV (e), and from -0.99 to 2.0 eV (f).

Figure 4.7. (a) Total and projected electronic density of states of ZrB<sub>2</sub>, and decomposed charge density on (11 $\bar{2}$ 0) plane in the energy range from -12.7 to -7.8 eV (b), from -8.7 to -3.1 eV (c), from -6.8 to -1.1 eV (d), from -4.1 to -1.1 eV (e), and from -2.7 to 0.6 eV (f), and from -0.03 to 4.0 eV (g).

Figure 4.8. (a) Total and projected electronic density of states of HfB<sub>2</sub>, and decomposed charge density on (11 $\bar{2}$ 0) plane in the energy range from -13.7 to -9.5 eV (b), from -9.4 to -4.1 eV (c), from -7.7 to -1.4 eV (d), from -4.8 to -1.4 eV (e), from -3.4 to 1.7 eV (f), and from -0.07 to 4.2 eV (g).

Figure 4.9. (a) Total and projected electronic density of states of NbB<sub>2</sub>, and decomposed charge density on (11 $\bar{2}$ 0) plane in the energy range from -14.1 to -10.0 eV (b), from -9.8 to -4.7 eV (c), from -7.7 to -2.4 eV (d), from -5.5 to -2.4 eV (e), from -4.4 to -1.2 eV (f), from -1.6 to 1.9 eV (g), from -0.7 to 3.5 eV (h), and from -0.6 to 3.8 eV (i).

Figure 4.10. (a) Total and projected electronic density of states of TaB<sub>2</sub>, and decomposed charge density on (11  $\bar{2}$ 0) plane in the energy range from -14.9 to -10.7 eV (b), from -10.5 to -5.3 eV (c), from -8.3 to -2.5 eV (d), from -6.1 to -2.5 eV (e), from -4.8 to -1.3 eV (f), from -1.7 to 2.1 eV (g), from -0.8 to 3.7 eV (h), and from -0.6 to 4.0 eV (i).

## Chapter 05

Figure 5.1. Representation of the repulsion and attraction forces as a function of interparticle distance. (a) When ceramic particles are suspended in a polar solvent, particle surfaces become charged depending on the chemistry and pH of the solution. M-OH groups represent surface hydroxyl group that reacts with acid or base. (b) The surface charge is balanced with a counterion cloud around the particle to provide electrical neutrality. Surface charge and the counterion cloud form the electrical double layer. (c) In addition to using the EDL to create repulsive forces between particles, steric and electrosteric mechanisms could be used by adding polymers or polyelectrolytes, respectively, which will adsorb on particle surfaces.

Figure 5.2. Schematic representation of the influence of volume fraction on the viscosity of suspensions as a function of shear rate. At low shear rate, Brownian motion dominates producing high-viscosity randomized structures. At high shear rates, particles line up in preferred flow structures and viscosity decreases.

Figure 5.3. Volume fraction of consolidated green body as a function of applied pressure for a well-dispersed suspension and attractive particle networks.

Figure 5.4. Classification of green near-net-shaping ceramic processing techniques.

Figure 5.5. Dry processing route to prepare UHTC components. The main challenge associated with current technology for preparing UHTCs is the need for high temperature and pressure to densify the materials. This leads to the use of sintering aids, which reduces the service performance and limits shapes to very simple geometries.

Figure 5.6. Colloidal processing route to prepare UHTC components. In addition to removing flaws related to powder aggregates and improvement in the homogeneity of the sample, the control of the interparticle forces leads to higher particle packing that reduces the temperature for sintering and the need of pressure. In addition, near-net-shaping allows the manufacturing of UHTC complex shapes.

Figure 5.7. Examples of colloidal shaping techniques. (a) Slip casting: the control of suspension rheology determines particle packing; the green body is formed by the removal of solvent by filtration; (b) Gelcasting: the green body strength is determined by the amount of monomer, crosslinker, initiator (and catalyst), and the solid content of the suspension; (c) Freeze casting: the green body microstructure is designed through control of ice growth, which is controlled by solid content, freezing temperature, freezing device, and cyoprotector addition.

Figure 5.8. Viscosity versus shear rate curves for  $ZrB_2$  suspensions prepared with different amounts of dispersant. The dispersant is Hypermer A70 and the solvent is cyclohexane. The volume fraction of solids is 50%.

Figure 5.9. Sintered density of ZrB<sub>2</sub> specimens as a function of processing route and sintering temperature. Densities of the green bodies for colloidal and dry processing routes were included as dashed horizontal lines for comparison.

Figure 5.10. Microstructure of ZrB<sub>2</sub> after sintering at 2100°C/1 h at different magnifications. (a and b) Colloidal processing and PS; (c and d) dry processing and PS; (e and f) colloidal processing and HP; (g and h) dry pressing and HP.

Figure 5.11. Shrinkage for ZrB<sub>2</sub> samples as a function of the processing route and type and temperature of sintering. (The linear shrinkage for PS samples showed in the graph represents the average of height and diameter of the samples tested; in the case of the HP samples, the linear shrinkage represents the average of their height only, since the diameter is constrained by die dimension.)

Figure 5.12. ZrB<sub>2</sub> Leading edge. (a) Green body produced by slip casting as-unmolded; (b) after pressureless sintering at 2100°C/1 h; (c) after oxytorch testing.

## Chapter 06

Figure 6.1. Relative density (rd) versus temperature (T) of ZrB<sub>2</sub>-based compositions using 5 vol% Si<sub>3</sub>N<sub>4</sub>/ or AlN, as sintering aid; onset temperatures and final relative densities are also reported on each curve.

Figure 6.2. ZrB<sub>2</sub> ceramic sintered using 5 vol% Si<sub>3</sub>N<sub>4</sub> as sintering aid: (a) SEM micrograph showing ZrB<sub>2</sub> (1), ZrO<sub>2</sub> (2), and BN (3), (b) high-resolution TEM micrograph of a grain-boundary phase.

Figure 6.3. Relative density (rd) versus temperature (T) of ZrB<sub>2</sub> sintered with 15 vol% of ZrSi<sub>2</sub>, MoSi<sub>2</sub>, or WSi<sub>2</sub>; onset temperatures and final relative densities are also reported on each curve.

Figure 6.4. Examples of microstructures of MB<sub>2</sub>-MeSi<sub>2</sub> composites: SEM micrographs showing (a) ZrB<sub>2</sub>-MoSi<sub>2</sub>, (b) ZrB<sub>2</sub>-WSi<sub>2</sub>, and (c) HfB<sub>2</sub>-ZrSi<sub>2</sub> (d) high-resolution TEM image of the interface between core and rim in ZrB<sub>2</sub>-TaSi<sub>2</sub> [41] and (e) the same interface showing low angle grain boundaries [41].

Figure 6.5. Isobaric multiphase equilibrium amount (kmol) versus temperature (T) calculated using HSC Chemistry v.6.1, 1 bar (a and b) or 1 mbar (c and d) of total equilibrium pressure; starting compositions (in kmol): 0.9 ZrO<sub>2</sub> + 0.8 B<sub>2</sub>O<sub>3</sub> (a and c), 0.9 ZrO<sub>2</sub> + 0.8 B<sub>2</sub>O<sub>3</sub> + 1.2 SiC + 0.05 SiO<sub>2</sub> (b and d).

Figure 6.6. Hot pressing of ZrB<sub>2</sub>-based compositions (ZS<sub>x</sub>) with varying SiC particulate content (x, vol%), compared to an only milled ZrB<sub>2</sub> powder (Z0): relative density (rd) versus temperature (T). Onset temperatures are indicated for each system.

Figure 6.7. Polished section of a hot-pressed ZrB<sub>2</sub>-20% SiC: ZrB<sub>2</sub>- (1), SiC- (2), ZrO<sub>2</sub>- (3) and SiO<sub>2</sub>-based glassy pockets (4).

Figure 6.8. Polished sections from hot-pressed ZrB<sub>2</sub>-based ceramics with 5 vol% (a) and 20 vol% SiC particulates (b).

Figure 6.9. (a) Relative density (rd) versus temperature (T) of ZrB<sub>2</sub> + 15 vol% SiC with (ZS15M), or without MoSi<sub>2</sub> (ZS15): onset temperatures are

indicated. Polished sections by SEM from hot-pressed ZS15 (b) and ZS15M (c) are shown.

Figure 6.10. Isobaric multiphase equilibrium amount (kmol) versus temperature ( $T$ ) calculated using HSC Chemistry v.6.1, 1 mbar (a) or 1 bar (b) of total equilibrium pressure, and  $0.9 \text{ ZrO}_2 + 0.8 \text{ B}_2\text{O}_3 + 1.2 \text{ SiC} + 0.4 \text{ B}_4\text{C} + 0.05 \text{ SiO}_2$  of starting composition (in kmol).

Figure 6.11. Relative density (rd) of  $\text{ZrB}_2$ -15SiC- $x$ WC composition (vol%) using high-energy milled ( $x = 2$  for ZSWC-HM up to  $T_{1 \text{ MAX}} = 1900^\circ\text{C}$ ) or only mixed  $\text{ZrB}_2$  ( $x = 5$  for ZSWC up to  $T_{2 \text{ MAX}} = 1930^\circ\text{C}$ ): (a) rd versus temperature ( $T$ ), (b) rd versus time ( $t$ ) at  $T_{1 \text{ MAX}}$  and  $T_{2 \text{ MAX}}$ . For ZSWC, uniaxial pressure was applied at the constant value of 30 MPa from RT, while in three steps for ZSWC-HM.

Figure 6.12. Polished regions by SEM of hot-pressed  $\text{ZrB}_2$ -15SiC-2WC composite (see ZSWC-HM in Fig. 6.11): (a) overall microstructure with  $\text{ZrB}_2$  (1), SiC (2), (W,Zr)B (3) and (b) magnification of  $\text{ZrB}_2$  cores (C) and (Zr,W) $\text{B}_2$  rim (R).

Figure 6.13. Strength ( $\sigma$ ) versus displacement ( $x$ ) curves recorded during 4-pt flexure test at  $1500^\circ\text{C}$  in air using different ceramics sintered by hot pressing (HP) or pressureless sintering (PS): (a)  $\text{HfB}_2$ -15 vol%  $\text{TaSi}_2$  (HF15Ta-HP),  $\text{HfB}_2$ -15 vol%  $\text{MoSi}_2$  (HF15Mo-HP),  $\text{ZrB}_2$ -20 vol%  $\text{MoSi}_2$  (Z20Mo-PS); (b)  $\text{ZrB}_2$ -15 vol% SiC (ZS15) with  $\text{B}_4\text{C}$ , WC, or  $\text{MoSi}_2$  as sinter additive.

Figure 6.14.  $\text{ZrB}_2$ -based composites hot-pressed with different  $\text{MeSi}_2$  (Me = Mo, Ta, W, Zr): average

flexural strength data ( $\sigma$ ) measured at different temperatures ( $T$ ). (a)  $\text{MeSi}_2 < 5$  vol% [13, 15, 33, 57, 80], (b)  $\text{MeSi}_2 > 10$  vol% [17, 19, 32]. For the sake of comparison, the composite containing SiC and  $\text{B}_4\text{C}$  is also reported, as one of the most refractory compositions.

Figure 6.15. Relative density (rd) versus temperature ( $T$ ) of pure HfC and HfC-15 vol%TaSi<sub>2</sub>; onset temperatures and final relative densities are also reported on each curve.

Figure 6.16. Examples of microstructures of MC sintered with MeSi<sub>2</sub>: SEM micrographs showing (a) HfC-MoSi<sub>2</sub> showing the cleaning effect of the silicide trapping HfO<sub>2</sub> and reduced to SiOC, (b) HfC-ZrSi<sub>2</sub> showing multiple core-shell grains, (c) TEM image showing dislocation between core and shell in TaC-TaSi<sub>2</sub>, (d) TEM image of a complex triple point in HfC-TaSi<sub>2</sub>, (e) HR-TEM showing clean interfaces in ZrC-TaSi<sub>2</sub>.

## Chapter 07

Figure 7.1. Schematic of the matrix microstructure formation mechanism of an RMI Cf-ZrC composite. (a) Heterogeneous nucleation sites of ZrC at 1950°C; (b) growth and grouping of ZrC grains at 1950°C; (c) coalescence of ZrC grains and trapping of liquid Zr at 1950°C; (d) growth of ZrC particles with liquid Zr inclusions and precipitation of  $\beta$ -Zr at 1950°C; (e) coalescence, growth of ZrC, and trapping of  $\beta$ -Zr as temperature decreases (above 1835°C); (f) transformation of liquid Zr into the eutectic phase at 1835°C; (g) phase transformation of  $\beta$ -Zr into  $\alpha$ -Zr at 1159°C and (h) final microstructure at room

temperature, showing ZrC particles with  $\alpha$ -Zr + ZrC and  $\alpha$ -Zr inclusions. The eutectic phase composed of  $\alpha$ -Zr + ZrC and  $\alpha$ -Zr serves as the grain boundaries in areas of densely distributed ZrC particles.

Figure 7.2. Comparison of C/C-UHTC composites ablated for a 30 s period under a  $3920 \text{ kW m}^{-2}$  heat flux: (a) C/C-ZrB<sub>2</sub>, (b) C/C-4ZrB<sub>2</sub>-1SiC, (c) C/C-1ZrB<sub>2</sub>-2SiC, (d) C/C-2SiC-1ZrB<sub>2</sub>-2HfC, (e) C/C-2SiC-1ZrB<sub>2</sub>-2TaC, and (f) C/C.

Figure 7.3. Cross section of a 30 mm diameter  $\times$  20 mm thick UHTC composite showing the distribution of UHTC powder.

Figure 7.4. UHTC composites after 60 s oxyacetylene torch testing.

Figure 7.5. The 30 mm diameter  $\times$  20 mm thick, Cf-HfB<sub>2</sub> composites after 60 s oxyacetylene torch testing at  $>2500^\circ\text{C}$  showing negligible surface erosion.

Figure 7.6. Electron image and EDS mapping on the cross section of a Cf-HfB<sub>2</sub> composite subjected to 60 s oxyacetylene torch testing. (a) Back scattered electron image, (b) carbon, (c) hafnium, and (d) oxygen. The bright top layer in (a) indicates HfO<sub>2</sub>.

Figure 7.7. Microstructure of polished sections of ZrB<sub>2</sub> plus 20 vol% SiC plus SCS-9a fibers composite showing (a) representative fiber distribution and (b) matrix porosity.

Figure 7.8. Microstructures of the ablated HfC coating on a C/C composite in different regions: (a) central; (b) transitional; and (c) outer ablation region.

Figure 7.9. Cross-sectional microstructure of a hybrid UHTC composite. The bonding between the

composite and monolith layers are fundamentally good as seen in the higher magnification image.

## Chapter 08

Figure 8.1. Room-temperature elastic modulus as a function of porosity for ZrB<sub>2</sub> (left) with and without sintering aids [11-14, 16, 17, 20-23, 25-29, 31-35, 37-39]. Line represents fitted relationship of elastic modulus to porosity according to Nielsen's relationship [40, 41].

Figure 8.2. Room-temperature flexure strength as a function of grain size for ZrB<sub>2</sub> (left) with and without sintering additives [11-14, 16-29, 31, 33, 34, 36, 37, 48]. Line is not fitted to data, and is meant to guide the eye.

Figure 8.3. Room-temperature flexure strength as a function of SiC cluster size (equivalent area diameter) for ZrB<sub>2</sub>-30 vol% SiC ceramics produced by hot pressing [7-9].

Figure 8.4. Room-temperature flexure strength, elastic modulus, and Vickers hardness as a function of maximum SiC cluster size (major axis of ellipse) for ZrB<sub>2</sub>-30 vol% SiC ceramics prepared by hot pressing. The dashed line indicates the microcracking threshold that occurs at an SiC cluster size of approximately 11.5 μm [8].

Figure 8.5. Room-temperature flexure strength [16, 22, 26, 37, 50, 57] and fracture toughness [16, 22, 26, 37, 50, 57] as a function of SiC concentration for ZrB<sub>2</sub>-SiC ceramics produced by hot pressing and pressureless sintering.

Figure 8.6. Thermally etched cross section of ZrB<sub>2</sub>-30 vol% SiC. The image shows the crack path from a

Vickers indent with arrows indicating predominantly transgranular fracture for the ZrB<sub>2</sub> grains and crack deflection near the ZrB<sub>2</sub>-SiC interfaces.

Figure 8.7. Elastic modulus as a function of additive content for selected hot-pressed ZrB<sub>2</sub>-based composites with SiC [16, 18, 26, 28, 52, 54, 63], MoSi<sub>2</sub> [14, 64-67], and ZrSi<sub>2</sub> [17] additives. Values have been corrected for porosity using a linear relationship and  $b = 2.0$ .

Figure 8.8. Room-temperature flexure strength and fracture toughness as a function of disilicide concentration for ZrB<sub>2</sub>-MeSi<sub>2</sub> ceramics produced by hot pressing [17, 27, 64].

Figure 8.9. Room-temperature flexure strength and fracture toughness as a function of SiC content for ZrB<sub>2</sub>-MoSi<sub>2</sub>-SiC and ZrB<sub>2</sub>-TaSi<sub>2</sub>-SiC ceramics [64, 88, 89].

Figure 8.10. Elevated-temperature elastic modulus of hot-pressed ZrB<sub>2</sub> with and without additives [20, 25, 29].

Figure 8.11. Elevated-temperature elastic modulus of hot-pressed ZrB<sub>2</sub>-SiC with and without additives [25, 69].

Figure 8.12. Elevated-temperature flexure strength of selected hot-pressed ZrB<sub>2</sub> ceramics with and without additives in air and argon [11-13, 20, 25, 29, 30].

Figure 8.13. Elevated-temperature flexure strength of selected hot-pressed ZrB<sub>2</sub>-SiC ceramics with and without additives in argon [25, 69, 90, 91].

Figure 8.14. Elevated-temperature flexure strength of selected hot-pressed ZrB<sub>2</sub>-SiC ceramics with various additives in argon [11, 15, 25, 67].

Figure 8.15. Elevated-temperature four-point flexure strength of selected ZrB<sub>2</sub>-MeSi<sub>2</sub> ceramics in air [25, 65-67, 79, 82, 83].

Figure 8.16. Elevated-temperature fracture toughness (CNB) of hot-pressed ZrB<sub>2</sub> and ZrB<sub>2</sub>-SiC ceramics [30, 69].

## Chapter 09

Figure 9.1. Thermochemical and experimental heat capacity (C<sub>p</sub>) values for ZrB<sub>2</sub> [8, 14-17, 24, 26, 27].

Figure 9.2. Historic thermal conductivity as a function of temperature for ZrB<sub>2</sub>. Data for Clougherty changed testing method at 1000°C [6-12].

Figure 9.3. Current thermal conductivity as a function of temperature values for ZrB<sub>2</sub>. <sup>a</sup>Data corrected for  $\rho$ . <sup>b</sup>Data corrected for C<sub>p</sub>. [13-18, 20-23] (Jason Lonergan, Missouri University of Science and Technology, personal communication).

Figure 9.4. Thermal conductivity as a function of temperature for ZrB<sub>2</sub> with solid solution additions. <sup>a</sup>Data corrected for  $\rho$  [18, 21-23].

Figure 9.5. Heat capacity as a function of temperature for HfB<sub>2</sub> [24, 27, 35].

Figure 9.6. Thermal conductivity as a function of temperature for historic and current HfB<sub>2</sub>. <sup>a</sup>Data corrected for  $\rho$  [9, 10, 14, 18, 37, 39, 40].

Figure 9.7. Thermal conductivity as a function of temperature for ZrB<sub>2</sub> with SiC additions ranging from 5 to 50 vol%. (Note: Clougherty changed testing methods at 1000°C.)<sup>a</sup>Data corrected for  $\rho$  [8, 14, 15, 18, 36, 41-45].

Figure 9.8. Thermal conductivity as a function of temperature for ZrB<sub>2</sub> with additions of carbon, MoSi<sub>2</sub>, or ZrC. Clougherty changed testing methods at 1000°C. [8, 11, 12, 20, 21, 48].

Figure 9.9. Thermal conductivity as a function of temperature for ZrB<sub>2</sub>-SiC-based composites with additions of, B<sub>4</sub>C, C (elemental, nanotubes (CNT) and graphite (Cg)), MoSi<sub>2</sub>, Si<sub>3</sub>N<sub>4</sub>, SiCw (whiskers), or ZrC. Clougherty changed testing methods at 1000°C.<sup>a</sup>Data corrected for  $\rho$  [8, 18, 36, 41, 43, 48, 60, 72].

Figure 9.10. Thermal conductivity as a function of temperature for HfB<sub>2</sub>-SiC with SiC contents ranging from 2 vol% to 30 vol%. Clougherty changed testing methods at 1000°C.<sup>a</sup>Data corrected for  $\rho$  [8, 14, 18, 28, 36, 39, 78].

Figure 9.11. Thermal conductivity as a function of temperature for HfB<sub>2</sub> with additions of B<sub>x</sub>C (x = 3 or 12), C, or SiC with C or B<sub>4</sub>C. Clougherty changed testing methods at 1000°C.<sup>a</sup>Data corrected for  $\rho$  [8, 18, 54, 75].

Figure 9.12. Total, electron, and phonon thermal conductivities as a function of temperature for ZrB<sub>2</sub> and HfB<sub>2</sub>.<sup>a</sup>Data corrected for  $\rho$  [15-17, 20, 79].

Figure 9.13. Thermal conductivities as a function of temperature for ZrB<sub>2</sub>-SiC and HfB<sub>2</sub>-SiC, including separation of the electron and phonon contributions

to total conductivity.<sup>a</sup>Data corrected for  $\rho$  [16, 20, 50, 84].

## Chapter 10

Figure 10.1. (a) Elastic constants for  $ZrB_2$  as a function of temperature as measured by Okamoto *et al.* [12] and (b) the average Young's modulus,  $E_{avg}$  (filled squares); shear modulus,  $G_{avg}$  (filled triangles); and bulk modulus,  $K$  (filled circles), as a function of temperature using the same data. Also shown are the variation of Young's modulus as measured in flexure by Neuman *et al.* (half-filled diamonds) [16] and Rhodes *et al.* (open diamonds) [17] and the variation of Young's modulus of  $ZrB_2$  as measured from the natural resonance frequency (open squares) [18].

Figure 10.2. Young's modulus versus temperature for a range of UHTCs. Closed symbols are measurements based on vibration, whereas open symbols were obtained from flexural tests. Data from Refs. [18, 20-23].

Figure 10.3. Hardness of two types of zirconium diboride (100% dense with addition of 20 vol% SiC and 90% dense with no additions) as a function of the size of the applied load. Data from Ref. [32].

Figure 10.4. Hardness as a function of load in a  $ZrB_2$  containing SiC and  $B_4C$ . Data taken from Ref. [32]. Where indents were apparently made in a single phase, they have been grouped accordingly.

Figure 10.5. TEM bright-field micrograph of a cross section through a Berkovich indent in  $ZrB_2$  containing SiC. It appears that the SiC has resisted deformation more and has been pushed into the  $ZrB_2$